Journal of Alloys and Compounds 503 (2010) 194–203

Contents lists available at ScienceDirect

Journal of Alloys and Compounds

journal homepage: www.elsevier.com/locate/jallcom

Studies of covalent amides for hydrogen storage systems: Structures and bonding of the $MAl(NH_2)_4$ phases with M = Li, Na and K

J.-B. Eymery[a], L. Truflandier[b], T. Charpentier[b], J.-N. Chotard[a], J.-M. Tarascon[a], R. Janot[a,*]

[a] Laboratoire de Réactivité et Chimie des Solides, UMR 6007 CNRS, Université de Picardie - Jules Verne, 33 rue St Leu, 80039 Amiens, France
[b] CEA, IRAMIS, SIS2M - Laboratoire de Structure et Dynamique par Résonance Magnétique, 91191 Gif-sur-Yvette, France

ARTICLE INFO

Article history:
Received 2 February 2010
Received in revised form 22 March 2010
Accepted 31 March 2010
Available online 6 May 2010

Keywords:
Amides
DFT calculations
Hydrogen storage
Infrared spectroscopy
Thermal analysis

ABSTRACT

Mixtures of metallic amides and LiH are studied as hydrogen storage materials. We show that the amides decomposition temperature decreases as the polarizing effect of the metallic cation increases, hence our interest for amides with strong polarizing cations such as Al^{3+}. Studying the $MAl(NH_2)_4$ phases with M = Li, Na and K, we tried to rationalize such metal-decomposition temperature dependence and found from IR spectroscopy investigations supported by DFT calculations that smaller is the alkali cation M^+, more the $Al(NH_2)_4$ and $M(NH_2)_4$ tetrahedra are interconnected in the crystal structures and higher is the decomposition temperature. Regarding applications, the possibility of using the $LiAl(NH_2)_4$–LiH mixture as a reversible hydrogen storage material is discussed. If such mixture is able to release up to 6.2 mass% of hydrogen at 130 °C, it is shown that the $LiAl(NH_2)_4$ decomposition leads to the formation of amorphous $LiAl(NH)_2$ imide, which is unfortunately metastable and exothermically transformed into $LiNH_2 + AlN$. This last reaction is highly problematic for hydrogen storage applications as it is fully irreversible and AlN does not react with hydrogen under moderate temperature and pressure conditions.

1. Introduction

Due to the growing interest for hydrogen as an energy vector, the development of a safe method for its storage is compulsory needed. If the advantages of using a solid-state hydrogen storage material have been demonstrated, none of the compounds already reported in the literature are able to satisfy both a high hydrogen gravimetric capacity (>6 mass%) and a low operating temperature (<150 °C). Among the large variety of hydrogen storage materials, alanates and borohydrides regain a lot of interest due to their lightweights. These compounds are often called complex hydrides, as they consist in covalent groups (AlH_4^- and BH_4^-, respectively), which are ionically bonded with alkali or alkaline-earth metals. More recently, another class of complex compounds has been investigated for their hydrogen storage capabilities: the amides and imides with NH_2^- and NH^{2-} covalent groups, respectively. These compounds cannot be called hydrides as nitrogen has a higher electronegativity than hydrogen (3.1 vs. 2.2 according to Allred–Rochow values) and, therefore, hydrogen is positively charged in these compounds.

The possibility of storing hydrogen using amide–imide systems has been initially put forward with the hydrogenation of lithium nitride [1–3]. It has been demonstrated that 6.5 mass% of hydrogen can be reversibly stored in the Li–N–H system according to this equation:

$$LiNH_2 + LiH \leftrightarrow Li_2NH + H_2 \quad (1)$$

The desorption reaction is endothermic with an enthalpy of about +50 kJ/mol H_2, which corresponds to a hydrogen equilibrium pressure of 1 bar around 280 °C [1]. Shortly after this pioneering work, additional experiments have clarified the reaction mechanism [4,5]. It has been shown by mass spectrometry that the hydrogen desorption process is mediated by the ammonia formation according to the following two-step reaction:

$$2LiNH_2 \rightarrow Li_2NH + NH_3 \quad (2)$$

$$LiH + NH_3 \rightarrow LiNH_2 + H_2 \quad (3)$$

In a first step, lithium amide is endothermically decomposed into lithium imide and ammonia and, then, ammonia quickly reacts with LiH to produce $LiNH_2$ and to release hydrogen. As the second step is highly exothermic (−43 kJ/mol), its rate is very fast and LiH acts actually as an ammonia getter. $LiNH_2$ formed in reaction (3) is also decomposed in his turn according to the same two-step process. Indeed, there is a continuous succession of reactions until all $LiNH_2$ is consumed and the final products are Li_2NH and H_2 as written in Eq. (1).

Following this study and with the goal of finding other metal–N–H systems with more suitable thermodynamic properties

* Corresponding author. Tel.: +33 3 22 82 79 01; fax: +33 3 22 82 75 90.
E-mail address: raphael.janot@u-picardie.fr (R. Janot).

0925-8388/$ – see front matter © 2010 Elsevier B.V. All rights reserved.
doi:10.1016/j.jallcom.2010.03.248

(e.g. 1 bar hydrogen equilibrium pressure at lower temperature), the Li–Mg–N–H system has been investigated [6–14]. The 1:2 $Mg(NH_2)_2$–LiH material is promising, as it can release 5.6 mass% of hydrogen, associated with the formation of the ternary $Li_2Mg(NH)_2$ imide upon desorption:

$$Mg(NH_2)_2 + 2LiH \leftrightarrow Li_2Mg(NH)_2 + 2H_2 \quad (4)$$

This reaction presents a nice reversibility with fast kinetics at 200 °C. Its equilibrium pressure is high at this temperature (about 35 bar), but this reaction is actually ideal from the thermodynamic point of view, as its enthalpy of 35 kJ/mol H_2 could lead to 1 bar equilibrium pressure at about 100 °C. Unfortunately, the absorption/desorption kinetics are slow below 200 °C and no reproducible catalytic effect has been reported to enhance these kinetics. The mechanism for reversible hydrogen storage in the Li–Mg–N–H system is not yet fully understood. Two different models are reported for the explanation of the desorption process: the first one is based on a solid–solid interaction between $H^{\delta+}$ in the amide and $H^{\delta-}$ in LiH leading to a direct hydrogen release [8,9], whereas the other one consists in an ammonia-mediated mechanism similar to the two-step process encountered with Li–N–H [10–13]. According to this second model, the hydrogen desorption kinetic of the Li–Mg–N–H system is governed by the decomposition rate of the $Mg(NH_2)_2$ amide.

With the aim of still decreasing the temperature for reversible hydrogen storage, we decided in our group to promote the covalent character of the metal–nitrogen bond, which means that we have studied amides of more electronegative metals. In a previous paper, we especially reported the interest of using the $LiAl(NH_2)_4$ compound [15]. This amide is rapidly decomposed in a single step at about 130 °C with the release of 2 mol of ammonia. We have shown that the mixing of this amide with an appropriate amount of LiH (in order to trap the NH_3 release) allows the preparation of a Li–Al–N–H system, which is able to desorb up to 6.2 mass% of hydrogen at 130 °C. The proposed reaction is as follows:

$$LiAl(NH_2)_4 + 4LiH \rightarrow LiAl(NH)_2 + 2Li_2NH + 4H_2 \quad (5)$$

This reaction is promising as the hydrogen desorption occurs at a temperature about 70 °C lower than that of the Li–Mg–N–H system previously reported in the literature.

In this paper, we report a relationship between the polarizing effects of the metallic cations and the force constants of the N–H covalent bonds of the corresponding amides due to a study by infrared spectroscopy. As a consequence, the decomposition temperatures of binary $M(NH_2)_x$ amides can be directly related to the polarizing effects of the M^{x+} cations. We give a further investigation on the thermal decomposition of $LiAl(NH_2)_4$ and we extend our study to the isotypal $MAl(NH_2)_4$ compounds with M = Na and K. The experimental IR spectra of the $MAl(NH_2)_4$ phases are especially interpreted due to Density Functional Theory (DFT) calculations allowing the simulation of IR spectra. Finally, the possibility of using the $LiAl(NH_2)_4$–LiH mixture as a hydrogen storage material is discussed.

2. Experimental

2.1. Synthesis

The $MAl(NH_2)_4$ amides are prepared by reaction in liquid ammonia at room temperature from the corresponding $MAlH_4$ alanates [16]. Commercial $LiAlH_4$ and $NaAlH_4$ powders (Aldrich, 95%, 40 μm) are used as precursors, whereas $KAlH_4$ is a laboratory-made sample prepared by ball-milling under hydrogen pressure of Al powder (Aldrich, 99%, 40 μm) and KH powder (previously obtained from a 30 mass% dispersion in mineral oil, Aldrich). KH and $KAlH_4$ powders show a good purity as all the reflections on their X-ray diffraction diagrams can be attributed to the desired phases. The equation for the synthesis of the $MAl(NH_2)_4$ amides is as follows:

$$MAlH_4 + 4NH_3 \rightarrow MAl(NH_2)_4 + 4H_2 \quad (6)$$

Due to the high air/moisture reactivity of the alanates and amides, the entire handling of the reactants and products is performed in a glove box filled with purified argon. The vapor pressure of ammonia being about 10 bar at 25 °C, the syntheses are carried out in a stainless steel reactor (250 cm^3 internal volume) equipped with an outlet for gas evacuation and loading. The protocol for the synthesis is as follows: (1) the alanate precursor is loaded into the reactor, which is outgassed under primary vacuum at room temperature for 1 h; (2) the reactor is connected to a pipe of gaseous ammonia, which has been previously purified by condensation onto sodium pieces; (3) a large excess of ammonia is solidified into the reactor (about 50 cm^3 of NH_3 for 1 g of $MAlH_4$) using a liquid nitrogen bath; (4) the ammonia gaseous flow is disconnected, the reactor is closed and the nitrogen bath is removed; (5) as the temperature increases, the ammonia melts and partially evaporates; and (6) after two days at room temperature, the hydrogen and unreacted ammonia are removed by pumping under primary vacuum at room temperature. Finally, the amide is collected in the glove box.

2.2. Characterizations

The structural determination is performed with a Bruker D8 diffractometer (Cu K_α radiation, λ = 1.5418 Å) equipped with a position sensitive detector. Due to the high moisture reactivity of the amides, an air-tightened sample holder with a beryllium window is used. This window is responsible for the presence of sharp Be reflections on the X-ray diffraction patterns. Besides X-ray diffraction, infrared spectroscopy is a powerful tool for the characterization of amides as the vibration bands associated to their covalent N–H bonds are well defined in both stretching and bending modes. Here the data collection is achieved in transmission using a Nicolet Avatar 370 DTGS spectrometer. The powder is mixed with KBr and pressed at 8 tons to make a pellet. The spectra are obtained from the accumulation of 50 acquisitions in the 400–4000 cm^{-1} range with a resolution of 0.5 cm^{-1}.

The thermal decompositions of the amides are carefully studied by combining differential scanning calorimetry, thermogravimetry and mass spectrometry. The DSC measurements are carried out with a Netzsch DSC204 calorimeter under argon flow using sealed aluminium crucibles with cap layers immediately perforated before the analysis to allow the gas release. A heating rate of 10 °C/min is used for all samples. The thermogravimetric study is managed with a Hiden IGA001 analyzer equipped with an antechamber allowing the sample loading without any exposure to air. Typically, 150 mg of sample is loaded into a stainless steel bucket and the sample weight is continuously monitored upon heating under vacuum up to 500 °C. TPD experiments (temperature-programmed-desorption coupled with a mass spectrometer) are also conducted in order to obtain a fast identification of the desorbed gases. A home-made device with a quadripolar mass spectrometer (VG scientific Ltd., QXK300) is used. About 10 mg of sample is put into a stainless steel tube (6 mm diameter), which is then outgassed under primary vacuum. The TPD curves are acquired at a heating rate of 10 °C/min and temperatures up to 500 °C; the ammonia emission being determined from the change in the m/z = 17 peak intensity.

2.3. Computational details

In order to better understand the experimental IR spectra of the $MAl(NH_2)_4$ phases and, especially assign different observed stretching N–H doublets to different NH_2^- groups present in the crystal structures, simulated IR spectra have been obtained due to the Density Functional Theory (DFT) approach. Calculations were realized using the Perdew–Burke–Ernzerhof (PBE) generalized gradient approximation (GGA) of the exchange-correlation functional [17]. The so-called "ultrasoft" pseudopotentials were used to describe the interaction of the valence electrons with the nuclei and core electrons [18]. Equilibrium structures were obtained by optimizing the ion positions within the experimental cell parameters using the BFGS quasi-Newton algorithm implemented in PWscf [19] with a force tolerance parameter of 0.01 eV/Å. Calculations were converged with respect to the kinetic energy cut-off used for the basis set expansion and to the k-point density needed for the Brillouin zone integration. A cut-off of 35 Ry and a Γ-centred 4 × 4 × 2 Monkhorst–Pack grid [20] were sufficient to achieve convergence.

Calculation of the infrared spectra was based on the vibrational frequencies (ω_n) and the corresponding eigen-modes ($\boldsymbol{u}^n$) derived from the dynamical matrix ($\boldsymbol{D}$) at the centre of the Brillouin zone ($\boldsymbol{q}$ = 0). Nevertheless, at the long-wave limit ($\boldsymbol{q} \rightarrow 0$), the dynamical matrix associated with polar material displays a non-analytic behaviour due to the long-range character of the Coulomb forces [21]. Within the framework of the density functional perturbation theory [22], $\boldsymbol{D}$ can be expressed as:

$$\boldsymbol{D}^{\boldsymbol{q}\rightarrow 0}_{k\alpha,k'\beta} = \boldsymbol{D}^{\mathrm{A},\boldsymbol{q}=0}_{k,\alpha,k'\beta} + \boldsymbol{D}^{\mathrm{NA},\boldsymbol{q}\rightarrow 0}_{k\alpha,k'\beta} \quad (i)$$

where the labels (k,k') and (α,β) run over the atoms in the unit cell and the three Cartesian directions, respectively. $\boldsymbol{D}^{\mathrm{A}}$ is the analytical component of the dynamical matrix calculated at the Γ point as the second derivative of the total energy with respect to the atomic displacements, whereas $\boldsymbol{D}^{\mathrm{NA}}$ is the non-analytical part accounting for vibrational excitations longitudinal to the normalized direction $\boldsymbol{q}$ [22]. The mode oscillator strength (I^n) of the infrared-active mode n in the direction $\boldsymbol{q}$ was

evaluated from:

$$I^n \sim \sum_{q} |f^n(q)|^2 \quad \text{with} \quad f^n_\alpha(q) = \sum_{k,\beta} Z_{k,\alpha\beta} \frac{u^n_{k,\beta}(q)}{\sqrt{M_k}} \qquad \text{(ii)}$$

where $Z_{k,\alpha\beta}$ and M_k are the Born effective charge tensor and the mass of the atom k, respectively. The former described the coefficient of proportionality between the macroscopic polarization per unit cell created along the direction b and a rigid displacement of the sub-lattice of the atom k in direction α [23]. Note that the eigenmodes (as well as the eigen-frequencies) are dependent of the q direction through the non-analytic part of the dynamical matrix. As a result, in order to compare the theoretical results with the experimental infrared data obtained on a powder (isotropic system, i.e. no preferential orientation), the intensity should be averaged over all directions of q. Here, we have considered six non-equivalent directions. Eigen-frequencies, eigen-modes and Born effective charge tensors were calculated using the PHONON code [19]. Finally, the theoretical spectra were convoluted by a Lorentzian function with a full width at half height of 2 cm^{-1} and transformed in the transmittance mode for a direct comparison with experiment.

3. Results and discussion

3.1. Evolution of the N–H bond force constant in metallic amides

The amides of alkali and alkaline-earth metals are well known and their infrared spectroscopic signatures have been discussed [24–27]. Their infrared spectra present a well-defined doublet in the 3180–3400 cm^{-1} range due to the symmetric and asymmetric stretching modes of the NH_2^- group, these modes being written ν_1 and ν_3, respectively. In a first approximation, the NH_2^- group can be considered isolated in the crystal lattice. As a result, the force constant of the N–H covalent bond can be calculated from the Hooke's law applied in this case to a tri-atomic non-linear molecule. The equation allowing the calculation of the N–H bond force constant K_r, expressed in N/cm (or mdyne/Å), is as follows:

$$K_r = \frac{2\pi^2 c^2}{N_A} \left[\frac{\nu_3^2}{\mu_H + 2\mu_N \sin^2 \alpha/2} + \frac{\nu_1^2}{\mu_H + 2\mu_N \cos^2 \alpha/2} \right] \times 10^{-5} \qquad \text{(iii)}$$

where π is the *pi* number, N_A is the Avogadro number, c is the speed of light (in cm/s), ν_1 and ν_3 are the wave numbers (in cm^{-1}), μ_H and μ_N are the reduced masses (in mol/g) and α is the H–N–H angle. The α angle has been taken equal to 104.6° for all compounds, which is the value commonly found for binary amides [28]. This angle is actually almost identical to that encountered within the H_2O molecule as in both cases we have a tetrahedral configuration with two non-bonding electron pairs.

In order to get a qualitative representation of the metal influence on the N–H bond force constant in alkali and alkaline-earth amides, we have plotted the evolution of K_r deriving from Eq. (iii) as a function of the polarizing effect of the metallic cations (cf. Fig. 1). Here, the polarizing effect is given by the Z/R_i^2 value, according to the Goldschmidt definition [29], with Z being the oxidation state of the metal and R_i being its ionic radius. The polarizing effect represents the potentiality of the cation to create an electric field and thus to deform the electronic cloud of the NH_2^- group and to modify the N–H bond force constant. For the calculations of Z/R_i^2, the ionic radii have been taken in the Shannon table, according to the coordination number of the metallic cations found in the amides crystal lattices: coordination number of 3 for Be^{2+}, 4 for Li^+, Na^+, Mg^{2+}, 6 for K^+, Rb^+, Ca^{2+}, Sr^{2+}, Ba^{2+} and 8 for Cs^+. The ionic radii and the polarizing effects of the cations are summarized in Table 1, together with the wave numbers of the N–H stretching modes (values given by Bouclier et al. [24,25]) and the calculated N–H bond force constants.

As observed in Fig. 1, the N–H bond force constant increases with the polarizing effect of the metallic cation. For a big cation with a low oxidation state (like Cs^+, Rb^+), the force constant is low meaning that the electronic cloud of the NH_2^- group is mainly localized on the nitrogen atom. On the contrary, a small cation with a high oxidation state (Be^{2+} and Mg^{2+}) has a strong polarizing effect, the electronic cloud is displaced towards the H atoms and the N–H bond force constant is high [25]. In other words, lower is the electronic density on the nitrogen atom; higher is the N–H bond force constant. The same observation is found by comparing for a same cation the N–H bond force constants of NH_3, NH_2^- and NH^{2-} groups [25]: for instance, the force constants calculated from infrared spectroscopy results are 6.35 N/cm for NH_3 (solid), 5.93 N/cm for $LiNH_2$ and 5.56 N/cm for Li_2NH. In this case, higher is the number of Li^+ cations, higher is the electronic density on the nitrogen atom and, as a consequence, lower is the N–H bond force constant.

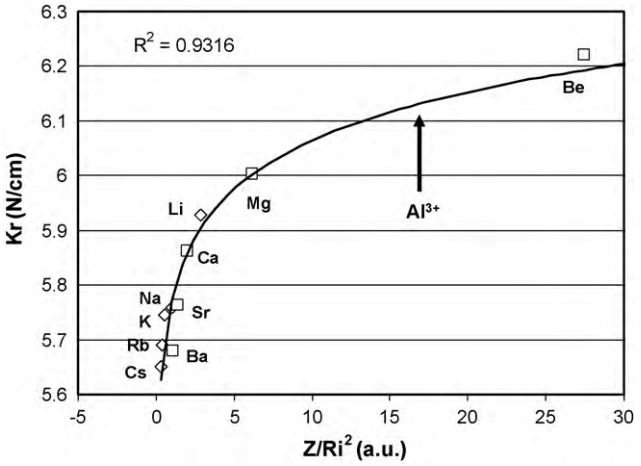

Fig. 1. N–H bond force constants of alkali and alkaline-earth amides as a function of the polarizing effects of the metallic cations. Al^{3+} is positioned in order to predict the N–H bond force constants of Al^{3+}-based amides.

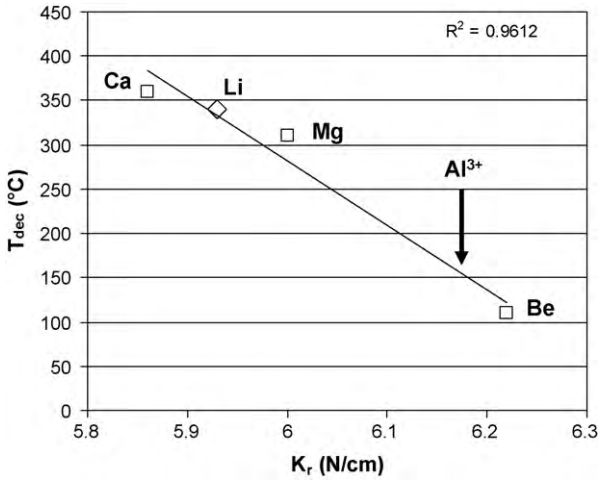

Fig. 2. Decomposition temperatures of binary amides as a function of the N–H bond force constants. Al^{3+} is positioned in order to predict the decomposition temperatures of Al^{3+}-based amides.

Fig. 2 presents the decomposition temperatures for various amides (decomposition through ammonia release with the formation of corresponding imides) as a function of the N–H bond force constant. The decomposition temperatures given in this figure have been experimentally measured in our laboratory from the maximum of the ammonia emission peaks recorded by TPD-MS (heating rate of 10 °C/min). It is clearly seen in Fig. 2 that higher is the N–H bond force constant (higher is the polarizing effect of the cation), lower is the decomposition temperature. The force constant of the N–H bond is actually a very relevant parameter to evaluate the amides stability. The calculation of the N–H bond force constant is an indirect estimation of the strength of the adjacent M–N bond: lower is the N–H bond force constant, stronger is the adjacent

Table 1
Stretching wave numbers and N–H bond force constants for amides of alkali and alkaline-earth metals. Polarizing effect of the metallic cations.

	Li^+	Na^+	K^+	Rb^+	Cs^+	Be^{2+}	Mg^{2+}	Ca^{2+}	Sr^{2+}	Ba^{2+}
ν_1 (cm^{-1})	3255	3210	3208	3190	3180	3329	3277	3233	3206	3186
ν_3 (cm^{-1})	3310	3260	3255	3242	3230	3394	3329	3295	3267	3240
K_r (N/cm)	5.93	5.76	5.75	5.69	5.65	6.22	6.00	5.86	5.76	5.68
R_i (Å)	0.59	0.99	1.38	1.52	1.74	0.27	0.57	1.00	1.18	1.35
Z/R_i^2	2.87	1.02	0.53	0.43	0.33	27.43	6.16	2.00	1.44	1.10

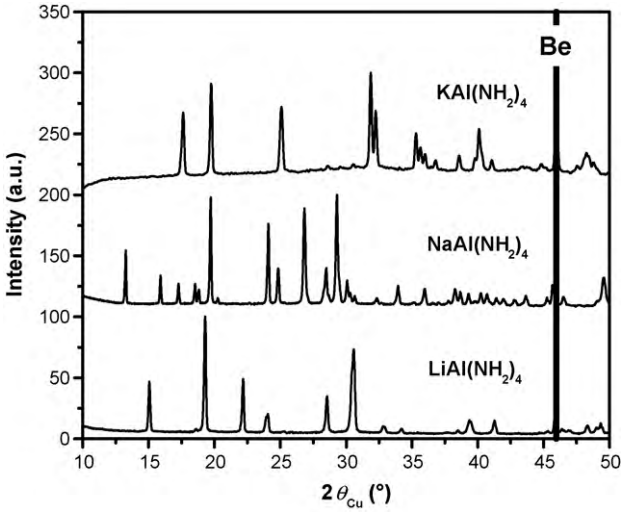

Fig. 3. X-ray diffraction diagrams of $MAl(NH_2)_4$ with M = Li, Na and K. The bold vertical line indicates a Be reflection of the sample holder.

M–N bond [24,25]. As the decomposition process of metallic amides occurs first through the breakings of M–N bonds (leading to NH_3 release), lower is the N–H bond force constant, higher is the amide decomposition temperature. It should have been very interesting to make a direct calculation of the M–N bond force constant, but the M–N vibrations are very difficult to identify by IR spectroscopy (due to a strong convolution at low wave numbers). The N–H vibrations being much easier identified, they have been used for the calculations of the N–H bond force constant and the prediction of the amides stability.

Although the decomposition of the Be^{2+}-based amides starts at very low temperatures (about 100 °C as shown in Fig. 2), their possible hydrogen storage properties when mixed with LiH were not investigated, due to the high toxicity of the Be-containing compounds and, in addition, due to their complex multi-step decomposition paths. This paper is indeed focused on aluminium-based amides as Al^{3+} is another strong polarizing cation: Z/R_i^2 is equal to 19.7 for Al^{3+} (ionic radius of 0.39 Å for a coordination number of 4). Such a high value should lead to Al^{3+}-containing amides with N–H bond force constants in the 6.1–6.2 N/cm range (cf. Fig. 1) and possibly with decomposition temperatures around 150 °C (cf. Fig. 2). If the $Al(NH_2)_3$ amide has been sometimes reported [30,31], its synthesis is very difficult. On the contrary, the $MAl(NH_2)_4$ amides with M being an alkali metal are easier synthesized and their structures are quite well established. The detailed study, both experimental and theoretical, of the infrared spectroscopic signatures of the $MAl(NH_2)_4$ phases is presented in the following.

3.2. Structures and bonding of the $MAl(NH_2)_4$ phases with M = Li, Na and K

The XRD diagrams of $LiAl(NH_2)_4$, $NaAl(NH_2)_4$ and $KAl(NH_2)_4$ are presented in Fig. 3. The vertical line at $2\theta = 45.9°$ corresponds to a reflection of the sample holder Be window. Except this reflection, all the lines can be indexed in the unit cells already reported in the literature for the $MAl(NH_2)_4$ phases: monoclinic with $P2_1/n$ space group for $LiAl(NH_2)_4$ [32], monoclinic with $P2_1/c$ space group for $NaAl(NH_2)_4$ [33] and orthorhombic with $C222_1$ space group for $KAl(NH_2)_4$ [34]. In all cases, the unit cells contain four $MAl(NH_2)_4$ formula units ($Z = 4$). The refined unit cells parameters found for our samples are given in Table 2. As expected, the unit cell volume increases with the size of the alkali metal: from 522 $Å^3$ for the phase with Li^+ up to 598 $Å^3$ for the phase with K^+ (representing a volume increase of 14.5%).

As the $MAl(NH_2)_4$ phases will be milled with LiH in order to prepare mixtures able to release hydrogen with a low ammonia contamination, their crystallinity will be strongly affected. Besides X-ray diffraction, infrared spectroscopy is a powerful tool for the characterization of such compounds with low crystallinity as this technique is a probe at the atomic scale. It was therefore important to establish relationships between the infrared spectra and the crystal structures for each $MAl(NH_2)_4$ phases, which means to try to give an attribution in the crystal lattices to different N–H vibrations bands (at least the stretching bands) observed on the experimental IR spectra. As we will see below the attribution of different N–H vibrational signatures cannot be realized without the support of first-principles calculations. Unfortunately, it is well known that proton positions suffer from a lack of accuracy when usual X-ray diffraction methods are used. This deficiency can yield to dramatic consequences on the calculated response functions like vibrational properties. Consequently, the structures of $LiAl(NH_2)_4$, $NaAl(NH_2)_4$ and $KAl(NH_2)_4$ have been optimized (i.e. the atomic positions were relaxed within the experimental cell parameters). The DFT-relaxed atomic positions can be found in Tables S1–S3 of the supporting information together with the principal bond lengths and angles (cf. Table S4). As expected, the DFT-calculated N–H bond lengths are significantly longer than the experimental ones: around 1.02 Å vs. solely 0.7–0.8 Å for the N–H distances obtained from XRD experiments. These results are consistent with previous theoretical works focusing on the $LiNH_2$ amide [35], where N–H bond lengths were predicted to be 1.03 Å, whereas the experimental values obtained from XRD are around 0.70–0.76 Å [28]. In a more recent experimental study, N–H distances of 0.94–0.99 Å were deduced from the refinement of neutron powder diffraction data [36], validating the sizable DFT corrections. These trends, i.e. N–H distance underestimation of XRD experiment compared to the less pronounced overestimation of the DFT geometry, are also depicted by the analysis of the H–N–H angle. The H–N–H experimental angles are within the interval of 67–108°, which is by far too low with regard to $LiNH_2$ (angles around 104°) [28]. DFT structure relaxation reduces the range of variation to 104–108° for the $MAl(NH_2)_4$ phases with M = Li, Na and K (cf. Table S4).

Fig. 4 presents the experimental IR spectra of $LiAl(NH_2)_4$ at room temperature and 77 K. In a first step, the IR spectrum was acquired at room temperature but surprisingly only five N–H stretching bands were observed, whereas an even number of bands is usually observed for amides as both symmetric and asymmetric stretchings lead to the presence of doublet(s) on the IR spectra. Actually, the thermal agitation at room temperature is responsible for the convolution of two bands around 3358 cm^{-1}. In order to overcome

Table 2
Space groups and unit cell parameters of $MAl(NH_2)_4$ phases with M = Li, Na and K.

	Space group	a (Å)	b (Å)	c (Å)	β (°)	V (Å^3)
$LiAl(NH_2)_4$	$P2_1/n$	9.5198(12)	7.3778(8)	7.4268(8)	90.271(7)	521.62(11)
$NaAl(NH_2)_4$	$P2_1/c$	7.3305(3)	6.0438(2)	13.1642(8)	94.017(4)	581.80(5)
$KAl(NH_2)_4$	$C222_1$	10.004(2)	5.8600(11)	10.2011(17)	90	598.0(2)

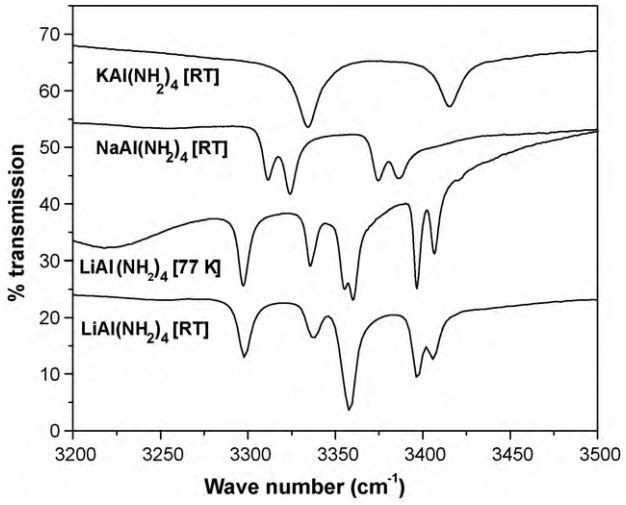

Fig. 4. Infrared spectra of $MAl(NH_2)_4$ with M = Li, Na and K. The spectra have been acquired at both room temperature and 77 K in the case of $LiAl(NH_2)_4$.

this issue, the spectrum was recorded immediately after dipping the KBr/sample pellet in liquid nitrogen. It is clearly evidenced in Fig. 4 that the band at 3358 cm^{-1} is split up at 77 K. Finally, six N–H stretching bands (3 doublets) are visible meaning that at least three NH_2^- groups are different in the crystal structure of $LiAl(NH_2)_4$. The IR spectra at room temperature of the $MAl(NH_2)_4$ phases with M = Na and K are also presented in Fig. 4. The spectra are very different with a single doublet for $KAl(NH_2)_4$, and two doublets for $NaAl(NH_2)_4$. In order to better understand this discrepancy, the unit cell lattices of the three phases are shown in Fig. 5 by especially highlighting the interconnectivity between the $Al(NH_2)_4$ tetrahedra.

A nice evolution of the structural arrangement is found depending on the size of the alkali metal cation. For the $KAl(NH_2)_4$ phase, the $Al(NH_2)_4$ tetrahedra are isolated in the lattice (cf. Fig. 5a) as the K–N bond distance is large (between 3.05 Å and 3.24 Å). The $Al(NH_2)_4$ tetrahedra are nearly perfect with a Al–N bond distance equal to 1.84 Å. The $KAl(NH_2)_4$ structure has been relaxed by DFT calculations and the IR spectrum has been simulated. Table 3 gathers the theoretically predicted (at 0 K) and experimentally observed (at 77 K) N–H stretching wave numbers for the $MAl(NH_2)_4$ phases with M = Li, Na and K. Despite the blue-shift of the predicted resonances, the accuracy of the DFT results is sufficient to unambiguously assign the experimentally observed N–H infrared bands, as demonstrated in Fig. 6, which exhibits the stretching regions (both calculated and experimental) for different compounds. The overall discrepancy observed between theory and experience (cf. Table 3) can have several origins which are mainly due to the approximation used to define the exchange-correlation functional [37]. For $KAl(NH_2)_4$, two nitrogen atoms are crystallographically different in the crystal lattice, meaning that two NH_2^- groups are slightly different in vibrational energy. These account for the presence of two doublets (4 bands) on the calculated IR spectrum (cf. Fig. 6a). However, due to thermal agitations, solely two bands at 3334–3415 cm^{-1} are visible on the experimental IR spectrum recorded at 77 K.

Moving to a smaller cation (e.g. Na^+), the distance between the alkali metal and the nitrogen atom is shorter: the Na–N bond dis-

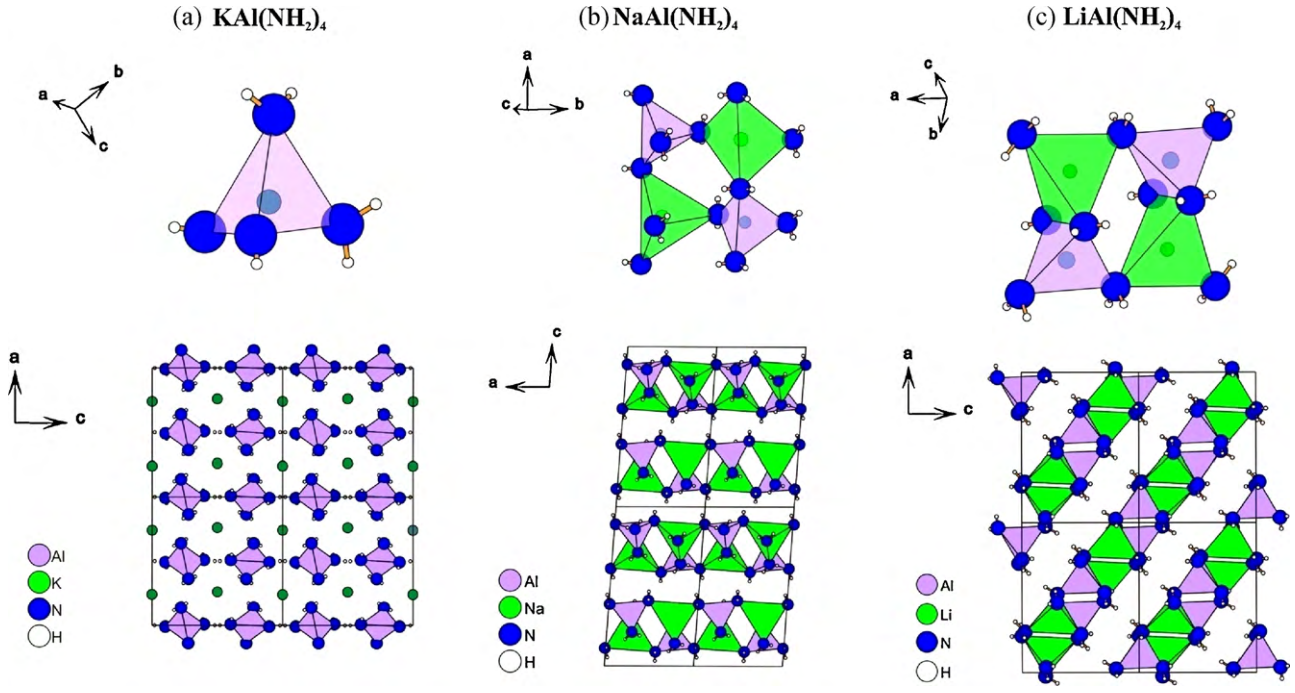

Fig. 5. Representation of the crystal structures of $MAl(NH_2)_4$ with M = Li, Na and K. The purple polyhedrons correspond to $Al(NH_2)_4$ tetrahedra, whereas the alkali cations are drawn in green. (For interpretation of the references to color in this figure legend, the reader is referred to the web version of this article.)

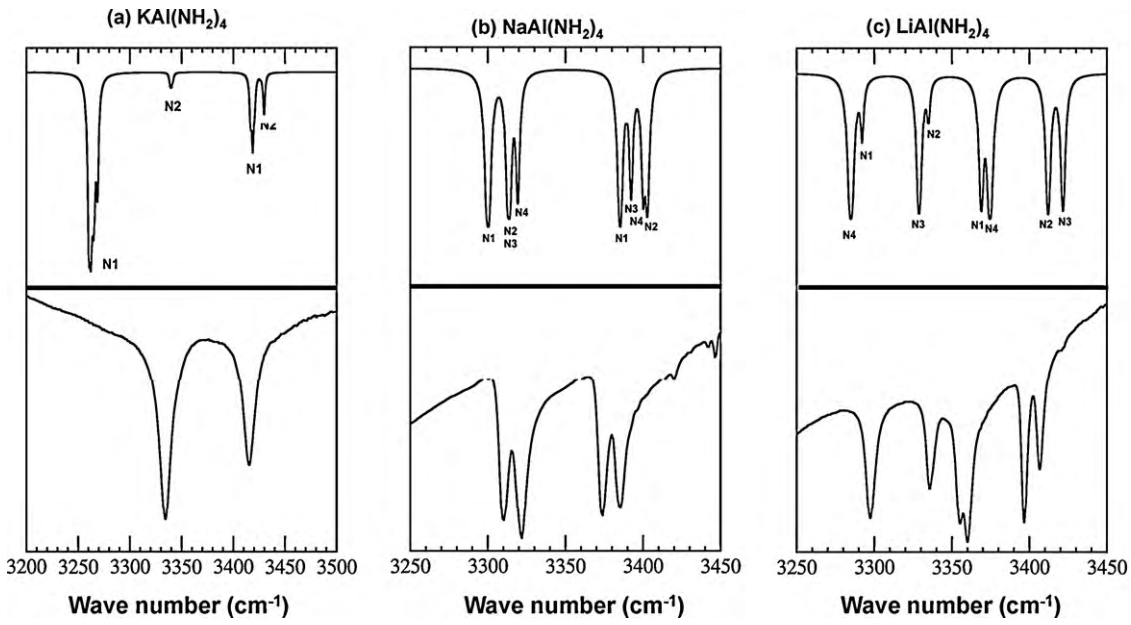

Fig. 6. Infrared spectra showing the N–H stretching regions for $MAl(NH_2)_4$ with M = Li, Na and K: DFT-simulated spectra at 0 K (top) and experimental spectra at 77 K (bottom). The DFT-simulated IR spectra have been shifted by 65 cm^{-1} towards the low wave number values. The N_x labels refer to different nitrogen atom positions given in the supporting information.

tance is in the 2.44–2.48 Å range for $NaAl(NH_2)_4$. The Na atoms have a coordination number of 4 with four NH_2^- groups surrounding them in a tetrahedral configuration. We can note that the Al–N bond distances in the $NaAl(NH_2)_4$ and $KAl(NH_2)_4$ phases are very similar, demonstrating that this parameter is not at the origin of the strong discrepancy between the IR spectra. Fig. 5b shows that the $Al(NH_2)_4$ and $Na(NH_2)_4$ tetrahedra are interconnected through vertices forming layers perpendicular to the *c* axis. The enchainment of tetrahedra in the $NaAl(NH_2)_4$ structure is responsible for the monoclinic distortion of the unit cell as opposed to orthorhombic $KAl(NH_2)_4$. Two different stretching doublets are observed on the infrared spectrum of $NaAl(NH_2)_4$, but their exact attributions were not easy. In order to overcome this issue, a simulated IR spectrum of $NaAl(NH_2)_4$ has been calculated using the DFT-relaxed structure (cf. Fig. 6b). Although a strong convolution already occurs at 77 K, a relatively nice agreement is found between the theoretical and experimental spectra of $NaAl(NH_2)_4$. Actually, four nitrogen atoms are crystallographically different in the crystal lattice, meaning that four NH_2^- groups are slightly different in vibrational energy. This accounts for the presence of four doublets on the calculated IR spectrum. However, due to very low differences in wave number (e.g. energy), the NH_2^- groups can be paired: we can distinguish the NH_2^- groups located at the edges of the layers (with one N–H bond perpendicular and the other one almost parallel to the layer) giving experimentally a IR doublet at 3324–3386 cm^{-1} and the NH_2^- groups rather located inside the layers (with the two N–H bonds pointing with an angle of about 38° vs. the layer surface) giving a doublet at 3312–3374 cm^{-1}.

Concerning $LiAl(NH_2)_4$, the Li–N bond distance ranges from 2.05 Å to 2.19 Å, a value about 14% shorter than the Na–N bond distance found in $NaAl(NH_2)_4$. As a result, the $Al(NH_2)_4$ and $Li(NH_2)_4$ tetrahedra are interconnected through both vertices and edges as shown in Fig. 5c. The enchainment of tetrahedra forms layers aligned along the [1 0 1] direction. The Al–N bond distance is around 1.84 Å as previously reported for the $KAl(NH_2)_4$ and $NaAl(NH_2)_4$ phases. Owing to the theoretical study made by DFT calculations, the three experimentally observed N–H stretching doublets have been identified (cf. Table 3). As for $NaAl(NH_2)_4$, the nitrogen atoms occupy four different crystallographic positions in the $LiAl(NH_2)_4$ lattice leading to four energetically different NH_2^- groups which can be gathered by pairs. Fig. 6c shows the calculated IR spectrum at 0 K with four doublets (top) and the experimental spectrum at 77 K (bottom) with only three visible doublets due to convolution. We have demonstrated that the NH_2^- groups for vertices interconnecting tetrahedra (corresponding to the nitrogen atoms labeled N1 and N4) are responsible for the two doublets at about 3298–3358 cm^{-1}, whereas the two doublets at higher wave numbers (higher energies) at about 3336–3400 cm^{-1} are related to the NH_2^- groups forming edges (e.g. nitrogen atoms labeled N2 and N3). We can note that the N–H bond force constant of the NH_2^- groups is strongly dependent of the connectivity: the force constant reaches 6.24 N/cm for the connecting edges, whereas the force constant is limited to 6.09 N/cm for the connecting vertices.

The crystal structures comparison for these $MAl(NH_2)_4$ phases shows a nice evolution, which can be resumed as follows. Smaller is the alkali metal cation, more the coordination polyhedra around the Al^{3+} and M^+ cations are interconnected to each other and more complex are the IR spectra. The $Al(NH_2)_4$ tetrahedra are isolated in the crystal lattice with K^+, whereas the tetrahedra are interconnected through vertices in the case of Na^+ and, finally, the tetrahedra are interconnected through both vertices and edges in the case of Li^+. Although not prepared in this study, $RbAl(NH_2)_4$ and $CsAl(NH_2)_4$ are also stable phases and their structures have been reported [38,39]. For these phases, the $Al(NH_2)_4$ tetrahedra are isolated leading to the presence of a single doublet on the infrared spectra, which is in good agreement with the observation given above for a large cation like K^+.

3.3. Thermal decomposition of the $MAl(NH_2)_4$ phases with M = Li, Na and K

The thermal decompositions (up to 500 °C) of the $MAl(NH_2)_4$ phases have been studied by combining TPD-MS and thermogravimetric experiments. Fig. 7 presents the curves of ammonia emission ($m/z = 17$) recorded by mass spectroscopy at a heating rate of 10 °C/min. As reported in a previous paper [15], the $LiAl(NH_2)_4$ decomposition leads to a strong ammonia release at 138 °C. This release has been quantified by thermogravimetry as shown in Fig. 8:

Table 3
Infrared-active N–H stretching modes of $MAl(NH_2)_4$ phases with M = Li, Na and K. Theoretically predicted and experimentally measured wave numbers.

$LiAl(NH_2)_4$				$NaAl(NH_2)_4$				$KAl(NH_2)_4$			
Theory ω (cm^{-1})	Exp. (cm^{-1})	Contribution[a]	Stretching mode	Theory ω (cm^{-1})	Exp. (cm^{-1})	Contribution[a]	Stretching mode	Theory ω (cm^{-1})	Exp. (cm^{-1})	Contribution[a]	Stretching mode
3350	3298	H7,H8 [N4]	sym	3365	3312	H1,H2 [N1]	sym	3331	3334	H3,H4 [N1]	sym
3357		H1,H2 [N1]	sym	3377		H5,H6 [N3]	sym				
3395	3336	H5,H6 [N3]	sym	3379	3324	H3,H4 [N2]	sym	3410		H1,H2 [N2]	sym
3400		H3,H4 [N2]	sym	3384		H7,H8 [N4]	sym				
3433	3355	H1,H2 [N1]	asym	3449	3374	H1,H2 [N1]	asym	3488	3415	H3,H4 [N1]	asym
3439	3360	H7,H8 [N4]	asym	3457		H5,H6 [N3]	asym				
3477	3397	H3,H4 [N2]	asym	3465	3386	H7,H8 [N4]	asym	3497		H1,H2 [N2]	asym
3487	3406	H5,H6 [N3]	asym	3468		H3,H4 [N2]	asym				

[a] Labels refer to Tables S1–S3 for $LiAl(NH_2)_4$, $NaAl(NH_2)_4$ and $KAl(NH_2)_4$, respectively. The nitrogen atom of the NH_2 group is given in parentheses.

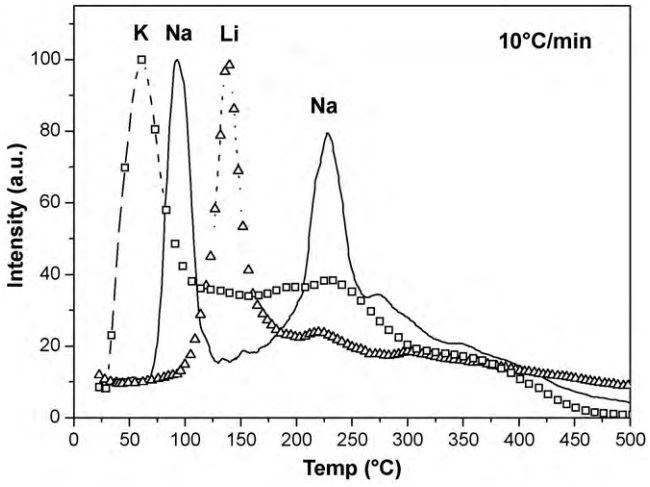

Fig. 7. Curves of ammonia emission ($m/z = 17$) of $MAl(NH_2)_4$ with M = Li, Na and K obtained by mass spectroscopy.

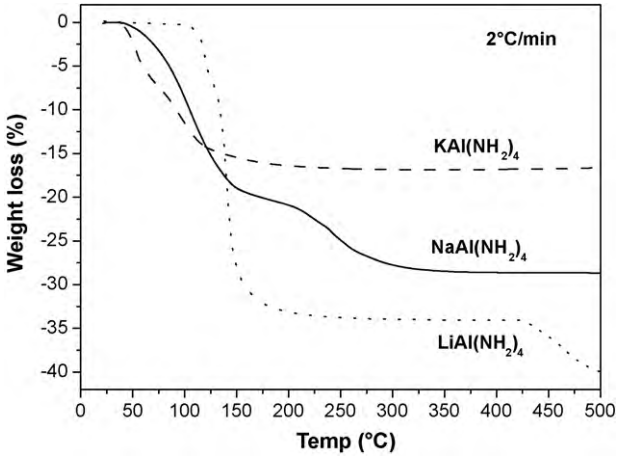

Fig. 8. Weight losses under primary vacuum of $MAl(NH_2)_4$ with M = Li, Na and K.

a weight loss of 34% is noticed, which is in good agreement with the release of 2 mol of ammonia per mole of $LiAl(NH_2)_4$. The following equation can be proposed for the decomposition at 138 °C [40]:

$$LiAl(NH_2)_4 \rightarrow LiAl(NH)_2 + 2NH_3 \quad (7)$$

An additional weight loss, which could be related to the $LiAl(NH)_2$ decomposition, is observed above 400 °C.

The decomposition process of $NaAl(NH_2)_4$ is different, since it occurs through two different steps as revealed in Fig. 7, which exhibits two peaks of ammonia release at 92 °C and 228 °C. This two-step process is confirmed by thermogravimetry as shown in Fig. 8. The total weight loss is about 29%, which also corresponds to the release of 2 mol of NH_3. The first step at 92 °C is probably related to the formation of an amino-imide with the $NaAl(NH_2)_2NH$ stoichiometry [31,41]. This complex compound is then further decomposed around 230 °C to form the final $NaAl(NH)_2$ imide according to the following two-step reaction:

$$NaAl(NH_2)_4 \rightarrow NaAl(NH_2)_2NH + NH_3 \rightarrow NaAl(NH)_2 + 2NH_3 \quad (8)$$

This two-step decomposition has been checked by DSC calorimetry (data not shown here) with the presence of two strong endothermic signals around 90 °C and 230 °C.

Finally, the ammonia release of $KAl(NH_2)_4$ occurs at a very low temperature with a peak maximum at 61 °C by mass spectroscopy (heating rate of 10 °C/min). The total weight loss for $KAl(NH_2)_4$

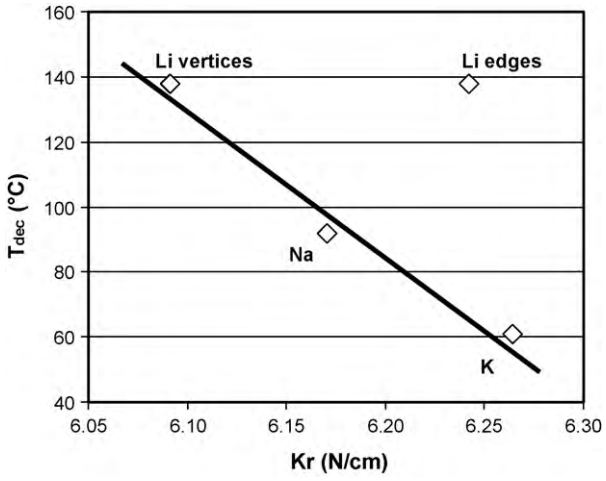

Fig. 9. Decomposition temperatures of the $MAl(NH_2)_4$ phases with M = Li, Na and K as a function of the N–H bond force constants. In the case of $LiAl(NH_2)_4$, two different force constant values are plotted according to two different types of NH_2^- groups present in the crystal lattice.

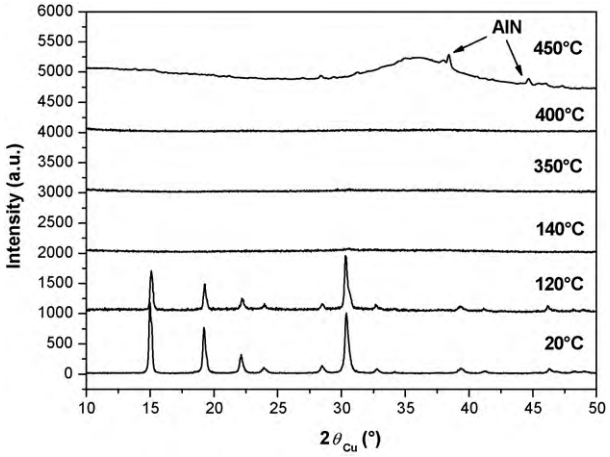

Fig. 10. X-ray diffraction diagrams of $LiAl(NH_2)_4$ desorbed under primary vacuum at different temperatures.

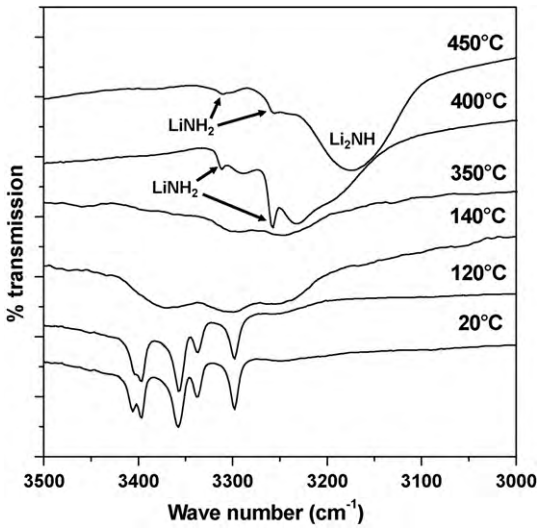

Fig. 11. Infrared spectra of $LiAl(NH_2)_4$ desorbed under primary vacuum at different temperatures.

reaches 17% corresponding to about 1.3 mol of NH_3. The weight loss curve presents fluctuations which could be related to the formation of several $KAl(NH_2)_x(NH)_y$ intermediate decomposition products. Anyway, the formation of $KAl(NH)_2$ imide for which the release of 2 mol of ammonia is expected does not seem to occur below 500 °C. This could be explained by some structural considerations based on the steric effect encountered with a large cation like K^+. From a structural point of view, the substitution of two NH_2^- groups by one NH^{2-} group strongly reduces the screening shell between large K^+ cations. As a result, a strong repulsion occurs and the structure is not stable. The same observation can be done with the binary amides–imides of alkali metals: on one hand, $LiNH_2$, $NaNH_2$ and KNH_2 are well reported and are stable compounds, whereas, on the other hand, only Li_2NH exists.

As a conclusion, the following tendency can be drawn for the $MAl(NH_2)_4$ phases: bigger is the alkali metal cation, more complex is the decomposition process, but lower is the first step decomposition temperature (138 °C with Li, 92 °C with Na and 61 °C with K). We tried to correlate this decomposition temperature with the N–H bond force constant calculated from the experimental infrared spectra. An interesting relationship is found when the doublet corresponding to the NH_2 interconnecting vertices are taken for the calculation of the N–H bond force constant of $LiAl(NH_2)_4$ as shown in Fig. 9. This suggests that the $LiAl(NH_2)_4$ decomposition with NH_3 formation occurs, from a crystallographic point of view, through the breaking of Al–N bonds at the vertices (release of NH_2) and N–H bonds at the edges (release of H). Similar to Fig. 2 about the binary amides with alkali and alkaline-earth metals, higher is the N–H bond force constant, lower is the decomposition temperature for the $MAl(NH_2)_4$ phases.

3.4. Identification of the $LiAl(NH_2)_4$ decomposition products

Due to its lightweight and its decomposition process in a single step, $LiAl(NH_2)_4$ has been mixed with LiH (in order to trap the NH_3 emission and to produce H_2) and the hydrogen storage properties of the $LiAl(NH_2)_4$–LiH mixture have been investigated. This study has been partially published in a previous paper [15]. It has been especially shown that the ball-milled 1:4 $LiAl(NH_2)_4$–LiH mixture can release up to 6.2 mass% of hydrogen at only 130 °C, a temperature about 70 °C lower than the 1:2 $Mg(NH_2)_2$–LiH system previously reported in the literature. Unfortunately, the reversibility of the hydrogen storage process was disappointing due to AlN formation upon cycling. In the following, we report a further investigation on the $LiAl(NH_2)_4$ decomposition process.

Due to both mass spectroscopy and thermogravimetric experiments, we have shown in the previous paragraph that $LiAl(NH_2)_4$ releases 2 mol of ammonia around 138 °C. The formation of a ternary $LiAl(NH)_2$ imide has been proposed in the literature [40] as written in reaction (7). The X-ray diffraction diagrams and IR spectra obtained after desorbing $LiAl(NH_2)_4$ under primary vacuum at different temperatures are presented in Figs. 10 and 11, respectively. No significant structural change is noticed up to 120 °C: the sole modification concerns the convolution of the infrared N–H stretching bands at 3397 cm^{-1} and 3406 cm^{-1}. At 140 °C, a total vanishing of the $LiAl(NH_2)_4$ XRD reflections is observed, which corroborates well with the experimentally measured amide decomposition temperature. More surprisingly, any new reflection appears on the XRD diagram suggesting the formation of a very amorphous material. We have visually checked that there is no melting effect and that the desorbed material remains in the solid state. The corresponding IR spectrum also reveals a strong amorphization: very weak vibrations bands are observed at lower wave numbers than those of $LiAl(NH_2)_4$, which could suggest an amide–imide transition. Longer durations of desorption were not relevant to improve the crystallinity of the desorbed material: actu-

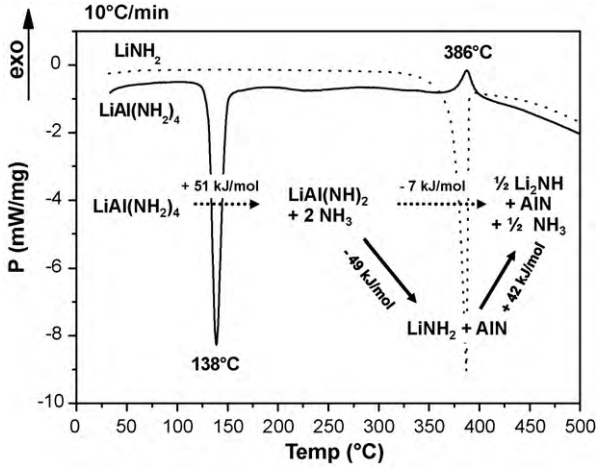

Fig. 12. DSC profiles of $LiAl(NH_2)_4$ (bold line) and $LiNH_2$ (dotted line) upon heating up to 500 °C.

ally, the very amorphous character of the $LiAl(NH)_2$ imide was already mentioned [40].

The amorphous character of the phase (or maybe the phases as we cannot certified that one single phase is present), obtained after ammonia release at about 130 °C, is persistent up to 350 °C as shown by both X-ray diffraction and IR spectroscopy. At 400 °C, new vibrations bands appear on the IR spectra: a doublet at 3257–3311 cm^{-1}, which can be unambiguously assigned to the N–H stretching deformations of $LiNH_2$, is visible. In addition, weak bands are also observed at about 3190 cm^{-1}, 3232 cm^{-1} and 3288 cm^{-1}. Their assignation is not easy, but they could be related to Li–Al imides. At the same temperature (400 °C), the X-ray diagram does not present any reflection showing the very amorphous state of the material. Heating up to 450 °C, a broad bump around 36° and two fine lines at 38.4° and 44.7° appear on the X-ray diagram ($2\theta_{Cu}$). The two fine lines can be indexed as the (1 1 1) and (2 0 0) reflections of face-centred-cubic AlN (a = 4.057 Å). On the other hand, the formation of Li_2NH is revealed by a broad band around 3180 cm^{-1} on the IR spectrum. The doublet at 3257–3311 cm^{-1}, already observed at 400 °C and assigned to $LiNH_2$, has strongly lost in intensity but it is still visible at 450 °C. According to these observations, the decomposition products of $LiAl(NH_2)_4$ mainly consist in AlN (according to X-ray diffraction) and Li_2NH (according to IR spectroscopy) at 450 °C, which could be summarized by the following equation as no other gas release than ammonia has been detected by mass spectroscopy:

$$LiAl(NH_2)_4 \rightarrow LiAl(NH)_2 + 2NH_3 \rightarrow 0.5Li_2NH + AlN + 2.5NH_3 \quad (9)$$

Such a decomposition process has been also investigated by DSC calorimetry as shown in Fig. 12. Two intense peaks are visible upon heating of $LiAl(NH_2)_4$: one endothermic peak at 138 °C and one exothermic peak at 386 °C. These two peaks can be easily related to the two steps of the reaction given above. The endothermic peak at 138 °C with an enthalpy $\Delta_r H^{411\,K}$ of +51 kJ/mol corresponds to the release of 2 mol of ammonia and to the formation of the amorphous $LiAl(NH)_2$ imide. The exothermic peak at 386 °C can be attributed to the formation of AlN and Li_2NH according to the second step of reaction (9). This step has an enthalpy $\Delta_r H^{659\,K}$ of −7 kJ/mol according to the DSC peak area.

Amazingly, the $LiNH_2$ decomposition occurs exactly at the same temperature of 386 °C (cf. DSC profile of $LiNH_2$ shown in Fig. 12 as a dotted line). The $LiNH_2$ decomposition, see reaction (2), is endothermic with an experimental enthalpy $\Delta_r H^{659\,K}$ of +42 kJ/mol (+84 kJ/mol NH_3) and leads to the formation of Li_2NH. This measured enthalpy is in very good agreement with values found in the literature [2]. Based on a simple thermodynamic cycle, the enthalpy of decomposition of $LiAl(NH)_2$ into $LiNH_2$ and AlN can be calculated as schematized in Fig. 12. An enthalpy $\Delta_r H^{659\,K}$ of −49 kJ/mol is found: this value is very negative emphasizing its high exothermic character and its irreversibility. Therefore, it can be concluded that amorphous $LiAl(NH)_2$ formed at 138 °C is metastable and is decomposed into $LiNH_2$ and AlN according to the following reaction:

$$LiAl(NH)_2 \rightarrow LiNH_2 + AlN \quad (10)$$

This reaction could explained the presence of the $LiNH_2$ stretching doublet on the IR spectra recorded at 400 °C and 450 °C (cf. Fig. 11), since such $LiNH_2$ existence is not expected from the two-step decomposition process written in reaction (9). At higher temperatures, $LiNH_2$ is decomposed in his turn to form Li_2NH and gives an extra ammonia release. This additional NH_3 release probably corresponds to the weight loss observed above 400 °C (cf. Fig. 8).

In the case of the mixture with LiH, it seems that the $LiAl(NH)_2$ stability is even lower as the attempts of rehydrogenation at 130 °C of the 1:4 $LiAl(NH_2)_4$–LiH ball-milled mixture have led to the fast growth of the AlN phase [15]. The $LiAl(NH)_2$ decomposition at low temperatures could be related to a direct interaction between $H^{\delta+}$ of $LiAl(NH)_2$ and $H^{\delta-}$ of LiH, leading to a strong destabilization [8,9].

4. Conclusions

A relationship between the polarizing effect of metallic cations and the decomposition temperature of binary amides (with alkali and alkaline-earth metals) has been found due to the calculation of the N–H bond force constants from infrared spectroscopy results. It has been shown that higher is the polarizing effect of the cation, lower is the decomposition temperature. In order to find amides with low decomposition temperatures, Al^{3+}-based amides have been studied, since Al^{3+} is a strongly polarizing cation. $MAl(NH_2)_4$ phases with M = Li, Na and K have been prepared by reaction in liquid ammonia from the corresponding $MAlH_4$ alanates.

The evolution of both crystal structures and infrared spectroscopic signatures of the $MAl(NH_2)_4$ phases has been discussed, according especially to the size of the alkali cations (Li^+, Na^+ and K^+). The IR bands of the $MAl(NH_2)_4$ experimental spectra have been identified by comparison with simulated IR spectra obtained due to a DFT study. It has been shown that smaller is the alkali cation, more the $Al(NH_2)_4$ and $M(NH_2)_4$ tetrahedra are interconnected to each other and more complex are the IR spectra. On the other hand, smaller is the alkali cation, higher is the decomposition temperature: $LiAl(NH_2)_4$ is decomposed at 138 °C, whereas the first step of the $NaAl(NH_2)_4$ and $KAl(NH_2)_4$ decompositions occurs at only 92 °C and 61 °C, respectively. Actually, the decomposition processes of $NaAl(NH_2)_4$ and $KAl(NH_2)_4$ are complex as the formations of $MAl(NH_2)_x(NH)_y$ amino-imides as intermediate products are noticed.

The $LiAl(NH_2)_4$ decomposition occurs in one step leading to the formation of amorphous $LiAl(NH)_2$ imide. We have shown that this imide is metastable and is exothermically transformed into $LiNH_2$ + AlN. This reaction is highly problematic for the hydrogen storage applications of the $LiAl(NH_2)_4$–LiH mixture as it is fully irreversible and AlN does not react with hydrogen under moderate temperature and pressure conditions.

Acknowledgements

This study has been carried out within the ALHAMO project (ANR-06-PANH-019). The PAN-H program of the ANR (Agence Nationale de la Recherche) is gratefully acknowledged for financial support. T. Charpentier and L. Truflandier also acknowledge the ANR for financial support through the Grant RMNSOLIDE-HR-HC project. Junxian Zhang and Fermin Cuevas (ICMPE-CNRS, Thiais)

are warmly thanked for the synthesis of $KAlH_4$ used as a precursor for the preparation of $KAl(NH_2)_4$.

Appendix A. Supplementary data

Supplementary data associated with this article can be found, in the online version, at doi:10.1016/j.jallcom.2010.03.248.

References

[1] P. Chen, Z. Xiong, J. Luo, J. Lin, K.L. Tan, Nature 420 (2002) 302–304.
[2] T. Ichikawa, S. Isobe, N. Hanada, H. Fujii, J. Alloys Compd. 365 (2004) 271–276.
[3] P. Chen, Z. Xiong, J. Luo, J. Lin, K.L. Tan, J. Phys. Chem. B 107 (2003) 10967–10970.
[4] Y.H. Hu, E. Ruckenstein, J. Phys. Chem. A 107 (2003) 9737–9739.
[5] T. Ichikawa, N. Hanada, S. Isobe, H. Leng, H. Fujii, J. Phys. Chem. B 108 (2004) 7887–7892.
[6] Z. Xiong, G. Wu, J. Hu, P. Chen, Adv. Mater. 16 (2004) 1522–1525.
[7] W. Luo, J. Alloys Compd. 381 (2004) 284–287.
[8] Z. Xiong, J. Hu, G. Wu, P. Chen, W. Luo, K. Gross, J. Wang, J. Alloys Compd. 398 (2005) 235–239.
[9] P. Chen, Z. Xiong, L. Yang, G. Wu, W. Luo, J. Phys. Chem. B 110 (2006) 14221–14225.
[10] H. Leng, T. Ichikawa, S. Hino, N. Hanada, S. Isobe, H. Fujii, J. Phys. Chem. B 108 (2004) 8763–8765.
[11] H. Leng, T. Ichikawa, S. Hino, T. Nakagawa, H. Fujii, J. Phys. Chem. B 109 (2005) 10744–10748.
[12] H. Leng, T. Ichikawa, H. Fujii, J. Phys. Chem. B 110 (2006) 12964–12968.
[13] R. Janot, J.B. Eymery, J.M. Tarascon, J. Power Sources 164 (2007) 496–502.
[14] J. Rijssenbeek, Y. Gao, J. Hanson, Q. Huang, C. Jones, B. Toby, J. Alloys Compd. 454 (2008) 233–244.
[15] R. Janot, J.B. Eymery, J.M. Tarascon, J. Phys. Chem. C 111 (2007) 2335–2340.
[16] A.E. Finholt, C. Helling, V.I. Imhof, L. Nielsen, E. Jacobson, Inorg. Chem. 2 (1963) 504–507.
[17] J.P. Perdew, K. Burke, M. Ernzerhof, Phys. Rev. Lett. 77 (1996) 3865–3868.
[18] D. Vanderbilt, Phys. Rev. B 41 (1990) 7892–7895.
[19] The PwSCF and PHONON codes are both implemented in the Quantum-ESPRESSO suite of programs. P. Giannozzi et al., http://www.quantum-espresso.org.
[20] H.J. Monkhorst, J.D. Pack, Phys. Rev. B 13 (1976) 5188–5192.
[21] P. Giannozzi, S. Gironcoli, P. Pavone, S. Baroni, Phys. Rev. B 43 (1991) 7231–7242.
[22] X. Gonze, C. Lee, Phys. Rev. B 55 (1997) 10355–10368.
[23] P. Ghosez, J.P. Michenaud, X. Gonze, Phys. Rev. B 58 (1998) 6224–6240.
[24] P. Bouclier, J. Portier, P. Hagenmüller, C.R. Acad. Sci. Paris 268 (1969) 720–723.
[25] P. Bouclier, Fr. thesis, Univ. Bordeaux, 1969.
[26] G. Linde, R. Juza, Z. Anorg. Allg. Chem. 409 (1974) 199–214.
[27] J.O. Bohger, R. Essman, H. Jacobs, J. Mol. Struct. 348 (1995) 325–328.
[28] H. Jacobs, R. Juza, Z. Anorg. Allg. Chem. 391 (1972) 271–279.
[29] V.M. Goldschmidt, Naturwiss 14 (1926) 477–485.
[30] E. Wiberg, A. May, Z. Naturforsch. 10 (1955) 230–232.
[31] R. Brec, Fr. thesis, Univ. Nantes, 1970.
[32] H. Jacobs, K. Jänichen, C. Hadenfeldt, R. Juza, Z. Anorg. Allg. Chem. 531 (1985) 125–139.
[33] H. Jacobs, B. Noecker, Z. Anorg. Allg. Chem. 619 (1993) 381–386.
[34] R. Brec, P. Palvadeau, P. Herpin, C.R. Acad. Sci. Paris 274 (1972) 266–268.
[35] K. Miwa, N. Ohba, S. Towata, Y. Nakamori, S. Orimo, Phys. Rev. B 71 (2005) 1951091–1951096.
[36] J.B. Yang, X.D. Zhou, Q. Cai, W.J. James, W.B. Yelon, Appl. Phys. Lett. 88 (2006) 419141–419143.
[37] S. Tosoni, F. Pascale, P. Ugliengo, R. Orlando, V.R. Saunders, R. Dovesi, Mol. Phys. 103 (2005) 2549–2558.
[38] P. Molinié, R. Brec, J. Rouxel, P. Herpin, Acta Cryst. B 29 (1973) 925–934.
[39] H. Jacobs, K.J. Jänichen, J. Less Common Met. 159 (1990) 315–325.
[40] J. Rouxel, R. Brec, C.R. Acad. Sci. Paris 262 (1966) 1070–1073.
[41] R. Brec, J. Rouxel, C.R. Acad. Sci. Paris 264 (1967) 512–515.